

PixelSNE: Visualizing Fast with Just Enough Precision via Pixel-Aligned Stochastic Neighbor Embedding*

Minjeong Kim
Korea University
mj1642@korea.ac.kr

Minsuk Choi
Korea University
mchoi@korea.ac.kr

Sunwoong Lee
Korea University
solomoj94@gmail.com

Jian Tang
University of Michigan
jjiant@umich.edu

Haesun Park
Georgia Tech
hpark@cc.gatech.edu

Jaegul Choo[†]
Korea University
jchoo@korea.ac.kr

ABSTRACT

Embedding and visualizing large-scale high-dimensional data in a two-dimensional space is an important problem since such visualization can reveal deep insights out of complex data. Most of the existing embedding approaches, however, run on an excessively high precision, ignoring the fact that at the end, embedding outputs are mapped into coarse-grained pixel coordinates in a limited screen space. Motivated by this observation and directly considering it in an embedding algorithm, we accelerate Barnes-Hut tree-based t-distributed stochastic neighbor embedding (BH-SNE), known as a state-of-the-art 2D embedding method, and propose a novel alternative called PixelSNE, a highly-efficient, screen resolution-driven 2D embedding method with a linear computational complexity in terms of the number of data items. Our experimental results show the significantly fast running time of PixelSNE by a large margin against BH-SNE, while maintaining the comparable embedding quality. Finally, the source code of our method is publicly available at <https://github.com/awesome-davian/pixelsne>.

CCS CONCEPTS

•Computing methodologies → Feature selection;

KEYWORDS

t-SNE; Barnes-Hut SNE; Dimension reduction; 2D embedding; Scatterplot; Visualization

ACM Reference format:

Minjeong Kim, Minsuk Choi, Sunwoong Lee, Jian Tang, Haesun Park, and Jaegul Choo. 1997. PixelSNE: Visualizing Fast with Just Enough Precision via Pixel-Aligned Stochastic Neighbor Embedding. In *Proceedings of ACM Woodstock conference, El Paso, Texas USA, July 1997 (WOODSTOCK'97)*, 9 pages.
DOI: 10.475/123_4

*Produces the permission block, and copyright information

[†]the corresponding author

Permission to make digital or hard copies of part or all of this work for personal or classroom use is granted without fee provided that copies are not made or distributed for profit or commercial advantage and that copies bear this notice and the full citation on the first page. Copyrights for third-party components of this work must be honored. For all other uses, contact the owner/author(s).

WOODSTOCK'97, El Paso, Texas USA

© 2016 Copyright held by the owner/author(s). 123-4567-24-567/08/06...\$15.00
DOI: 10.475/123_4

1 INTRODUCTION

Visualizing high-dimensional data in a two-dimensional (2D) or three-dimensional (3D)¹ scatterplot is an effective approach that can reveal deep insights about data. Through such visualization, one can obtain the idea about the relationships among clusters as well as those of individual data, e.g., similar or outlying clusters and/or data items.

To generate a scatterplot given high-dimensional data, one can apply various dimension reduction or low-dimensional embedding approaches including traditional methods (e.g., principal component analysis [9] and multidimensional scaling [11, 12]) and recent manifold learning methods (e.g., isometric feature mapping [20], locally linear embedding [18], and Laplacian Eigenmaps [2]).

These methods, however, do not properly handle the significant information loss due to reducing high dimensionality down to two or three, and in response, an advanced dimension reduction technique called t-distributed stochastic neighbor embedding (t-SNE) [22] has been proposed, showing its outstanding advantages in generating 2D scatterplots. A drawback of t-SNE is its significant computing time against a large number of data items, e.g., the computational complexity of $O(n^2)$, where n represents the number of data items. Although various approximation techniques attempting to accelerate its algorithm have been proposed, e.g., Barnes-Hut SNE (BH-SNE) [21] with the complexity of $O(n \log n)$, it still takes much time to apply them to large-scale data.

To tackle this issue, this paper proposes the novel framework that can significantly accelerate the 2D embedding algorithms in visualization applications. The proposed framework is motivated by the fact that most embedding approaches compute the low-dimensional coordinates with an excessive precision, e.g., a double precision with 64-bit floating point representation, compared to the limited precision that our screen space has. For instance, if our screen space has 1024×768 pixels, then the resulting coordinates computed from an embedding algorithm will be mapped with 1024 and 768 integer levels of x and y coordinates, respectively. Moreover, when making sense of a 2D scatterplot, human perception does not often require a high precision from its results [5].

Leveraging this idea of the just enough precision for our screen and human perception to the above-mentioned state-of-the-art method, BH-SNE, we propose a significantly fast alternative called pixel-aligned SNE (PixelSNE), which shows more than 5x fold

¹This paper discusses only the 2D embedding case, but our proposed approach can be easily extended to the 3D case.

speedup against BH-SNE for 421,161 data item of News aggregator dataset. In detail, by lowering and matching the precision used in BH-SNE to that of pixels in a screen space, PixelSNE directly optimizes 2D-coordinates in the screen space with a pre-given resolution.

In this paper, we describe the mathematical and algorithmic details of how we utilized the idea of a pixel-based precision in BH-SNE and present the extensive experimental results that show the significantly fast running time of PixelSNE by a large margin against BH-SNE, while maintaining the the embedding quality.

Generally, our contributions can be summarized as follows:

1. We present a novel framework of a pixel-based precision driven by a screen space with a finite resolution.
2. We propose a highly-efficient 2D embedding approach called PixelSNE by leveraging our idea of a pixel-based precision in BH-SNE.
3. We perform extensive quantitative and qualitative analyses using various real-world datasets, showing the significant speedup of our proposed approach against BH-SNE along with a comparable quality of visualization results.

2 RELATED WORK

Dimension reduction or low-dimensional embedding of high-dimensional data [24] has long been an active research area. Typically, most of these methods attempt to generate the low-dimensional coordinates that maximally preserve the pairwise distances/similarities given in a high-dimensional space. Such low-dimensional outputs generally work for two purposes: (1) generating the new representations of original data for improving the desired performance of a downstream target task, such as its accuracy and/or computational efficiency, and (2) visualizing high-dimensional data in a 2D scatterplot for providing humans with the in-depth understanding and interpretation about data.

Widely-used dimension reduction methods used for visualization application include principal component analysis (PCA) [9], multidimensional scaling [11, 12], Sammon mapping [17], generative topographic mapping [3], and self-organizing map [10]. While these traditional methods generally focus on preserving global relationships rather than local ones, a class of nonlinear, local dimension reduction techniques called manifold learning [14] has been actively studied, trying to recover an intrinsic curvilinear manifold out of given high-dimensional data. Representative methods are isometric feature mapping [20], locally linear embedding [18], Laplacian Eigenmaps [2], maximum variance unfolding [27], and autoencoder [8].

Specifically focusing on visualization applications, a recent method, t-distributed stochastic neighbor embedding [22], which is built upon stochastic neighbor embedding [7], has shown its superiority in generating the 2D scatterplots that can reveal meaningful insights about data such as clusters and outliers. Since then, numerous approaches have been proposed to improve the visualization quality and its related performances in the 2D embedding results. For example, a neural network has been integrated with t-SNE to learn the parametric representation of 2D embedding [15]. Rather than the Euclidean distance or its derived similarity information,

other information types such as non-metric similarities [23] and relative ordering information about pairwise distances in the form of similarity triplets [25] have been considered as the target information to preserve. Additionally, various other optimization criteria and their optimization approaches, such as elastic embedding [4] and NeRV [26], have been proposed.

The computational efficiency and scalability of 2D embedding approaches has also been widely studied. An accelerated t-SNE based on the approximation using the Barnes-Hut tree algorithm has been proposed [21]. Gisbrecht et al. proposed a linear approximation of t-SNE [6]. More recently, an approximate, but user-steerable t-SNE, which provides interactions with which a user can control the degree of approximation on user-specified areas, has also been studied [16]. In addition, a scalable 2D embedding technique called LargeVis [19] significantly reduced the computing times with a linear time complexity in terms of the number of data items.

Even with such a plethora of 2D embedding approaches, to the best of our knowledge, none of the previous studies have directly exploited the limited precision of our screen space and human perception for developing highly efficient 2D embedding algorithms, and our novel framework of controlling the precision in return for algorithm efficiency and the proposed PixelSNE, which significantly improves the efficiency of BH-SNE, can be one such example.

3 PRELIMINARIES

In this section, we introduce the problem formulation and the two existing methods, t-distributed stochastic neighbor embedding (t-SNE) and its efficient version called Barnes-Hut SNE (BH-SNE).

3.1 Problem Formulation

A 2D embedding method takes a set of high-dimensional data items, $\mathcal{X} = \{x_i \in \mathbb{R}^D\}_{i=1,2,\dots,N}$, where N is the number of data items and D is the original dimensionality, and gives their 2D (low-dimensional) embedding, $\mathcal{Y} = \{y_i \in \mathbb{R}^2\}_{i=1,2,\dots,N}$, as an output. Given a screen of resolution $r_1 \times r_2$, where r_1 and r_2 , the x - and y -axis resolutions, respectively, are positive integers, the scatterplot is generated by transforming \mathcal{Y} to their corresponding (zero-based) pixel coordinates

$$\mathcal{Z} = \left\{ [z_i] : z_i = \begin{bmatrix} z_{i,1} \\ z_{i,2} \end{bmatrix} \in \mathbb{R}^2, \right\}_{i=1,2,\dots,N} \quad \text{where} \quad (1)$$

$$0 \leq z_{i,d} < r_d, \forall d \in \{1, 2\}. \quad (2)$$

3.2 t-Distributed Stochastic Neighbor Embedding (t-SNE)

t-SNE embeds high-dimensional data into a low-dimensional space by minimizing the differences between the joint probability distribution representing pairwise relationships in \mathcal{X} and its counterpart in \mathcal{Y} . In detail, t-SNE computes the Euclidean pairwise distance matrix $D_{\mathcal{X}} \in \mathbb{R}^{N \times N}$ of \mathcal{X} and then converts it to the high-dimensional joint probability matrix $P \in \mathbb{R}^{N \times N}$ using a Gaussian kernel.

Next, given randomly initialized \mathcal{Y} , t-SNE computes the Euclidean pairwise distance matrix $D_{\mathcal{Y}} \in \mathbb{R}^{N \times N}$ and then converts it to a low-dimensional joint probability matrix $Q \in \mathbb{R}^{N \times N}$ using a Student's t -distribution. To be specific, the (i, j) -th component $q_{ij}^{(t)}$

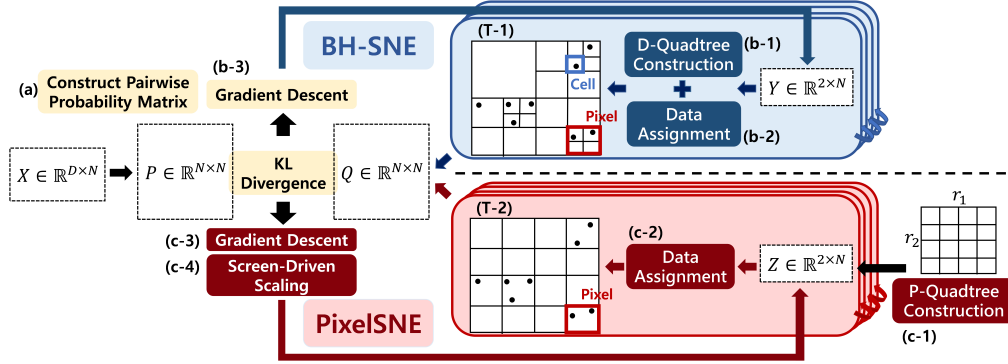


Figure 1: Overview of the proposed PixelSNE in comparison with the original Barnes-Hut SNE (BH-SNE)

of $Q^{(t)}$ at iteration t , which represents the similarity between $y_i^{(t)}$ and $y_j^{(t)}$ in a probabilistic sense, is computed as

$$q_{ij}^{(t)} = \left(\left(1 + \|y_i^{(t)} - y_j^{(t)}\|_2^2 \right) Z^{(t)} \right)^{-1} \quad (3)$$

where $Z^{(t)} = \sum_{k \neq l} \left(1 + \|y_i^{(t)} - y_j^{(t)}\|_2^2 \right)^{-1}$.

The objective function of t-SNE is defined using the Kullback-Leibler divergence between P and Q as

$$C = KL(P||Q) = \sum_{i \neq j} p_{ij} \log \frac{p_{ij}}{q_{ij}}, \quad (4)$$

and t-SNE iteratively performs gradient-descent update on \mathcal{Y} where the gradient with respect to y_i is computed [21] as

$$\begin{aligned} \frac{\partial C}{\partial y_i^{(t)}} = & 4(F_{attr} + F_{rep}) = 4 \left(\sum_{j \neq i} p_{ij} q_{ij}^{(t)} Z^{(t)} (y_i^{(t)} - y_j^{(t)}) \right. \\ & \left. - \sum_{j \neq i} (q_{ij}^{(t)})^2 Z^{(t)} (y_i^{(t)} - y_j^{(t)}) \right). \end{aligned} \quad (5)$$

Note that every data point exerts an attraction and an repulsion forces to one another based on the difference between the two pairwise joint probability matrices P and Q .

3.3 Barnes-Hut-SNE (BH-SNE)

While t-SNE adopts a brute-force approach with the computational complexity $\mathcal{O}(N^2)$ considering all the pairwise relationships, BH-SNE adopts two different tree-based approximation methods to reduce this complexity. The first one called the vantage-point tree [28] approximately computes $D_{\mathcal{X}}$ and then P as sparse matrices by ignoring small pairwise distances as zeros (Fig. 1(a)). This approximation reduces the complexity $\mathcal{O}(N^2)$ of computing $D_{\mathcal{X}}$ and P to $\mathcal{O}(uN \log N)$ where u is a pre-defined parameter of perplexity and $u \ll N$. Accordingly, involving only those nonzero p_{ij} 's in the sparse matrix P , the complexity of computing F_{attr} in Eq. (5) reduces to $\mathcal{O}(uN)$.

When it comes to optimizing low-dimensional coordinates (Fig. 1(b)), BH-SNE adopts Barnes-Hut algorithm [1] to compute F_{rep} in Eq. (5). When $\|y_i - y_j\| \approx \|y_i - y_k\| \gg \|y_j - y_k\|$, the forces of y_j and y_k to y_i are similar to each other when computing the gradient. Based

on this observation, BH-SNE uses Barnes-Hut algorithm to find a single representative point of multiple data points used for gradient update. For example, if we set the representative data point of y_j and y_k as y_s , then the low-dimensional joint probability q_{is} can be used to substitute each of q_{ij} and q_{ik} .

To dynamically obtain the representative points y_s 's, BH-SNE constructs a quadtree at each iteration, recursively splitting the 2D region that contains y_i 's into four pieces. Each node, which we call a cell c , contains the following information:

1. the boundary $\mathcal{B}_d^{(c)}$ about its corresponding 2D region, i.e.,

$$\mathcal{B}_d^{(c)} = [b_{min,d}^{(c)}, b_{max,d}^{(c)}] \text{ for } d = 1, 2 \quad (6)$$

2. the set \mathcal{Y}_c of y_i 's contained in c , i.e.,

$$\mathcal{Y}_c = \{y_i : y_{i,d} \in \mathcal{B}_d^{(c)} \text{ for } d = 1, 2\}, \quad (7)$$

and its cardinality, $N_c = |\mathcal{Y}_c|$, and

3. the center of mass, y_c , of y_i 's in c , i.e.,

$$y_c = \frac{1}{N_c} \sum_{y_i \in \mathcal{Y}_c} y_i \quad (8)$$

Given $y_i^{(t)}$ at iteration t , BH-SNE starts by forming a root node c_{root} , containing all the $y_i^{(t)}$'s, by setting $\mathcal{Y}_{c_{root}} = \mathcal{Y}$ in Eq. (7) and

$$b_{min,d}^{(c_{root})} = \min_i y_i^{(t)} \text{ and} \quad (9)$$

$$b_{max,d}^{(c_{root})} = \max_i y_i^{(t)} + \epsilon, \forall d \in \{1, 2\}, \quad (10)$$

where ϵ is a small number in Eq. (6). BH-SNE then recursively splits c into four (equally-sized) quadrant cells located at "northwest", "northeast", "southwest", and "southeast" by setting their boundaries accordingly, assigning $y^{(t)}$'s to these child cells based on the boundary information in Eq. (7), and computing their centers of mass. As assigning $y^{(t)}$'s one by one to the tree, the quadtree grows until each leaf node contains at most a single $y_i^{(t)}$.

Afterwards, when computing the gradient with respect to y_i in Eq. (5) (Fig. 1(b-3)), BH-SNE traverses the quadtree via depth-first search to determine whether y_c can work as the representative point of those contained in c based on the criterion

$$r_c / \|y_i - y_c\|_2^2 < \theta, \quad (11)$$

where r_c represents the diagonal length of the region of c and θ is a threshold parameter. Once finding y_c satisfying this criterion, the term $-q_{ij}^2 Z(y_i - y_j)$ in Eq. (5) for those points contained in c is approximated as $-N_c q_{i,c}^2 Z(y_i - y_c)$, thus reducing the computational complexity of F_{rep} in Eq. (5) to $O(N \log N)$.

4 PIXEL-ALIGNED SNE (PIXELSNE)

In this section, we present our PixelSNE, which significantly reduces the computational time of BH-SNE.

4.1 Pixel-Aligned Barnes-Hut Tree

A major novelty of PixelSNE originates from the fact that it directly considers the screen-space coordinates z_i (Eq. (1)) instead of y_i . That is, PixelSNE utilizes the two properties of z_i during its optimization process: (1) the range of $z_{i,d}$ remains fixed as $[0, r_d]$ for $d = 1, 2$ throughout algorithm iterations (Eq. (2)) and (2) the precision of z_i is limited by the screen space resolution. Utilizing these characteristics, we accelerate the Barnes-Hut tree construction as the assignment process of z_i 's to cells as follows. For clarification, we denote our accelerated quadtree algorithm of PixelSNE as a pixel-aligned quadtree (P-Quadtree) while we call the original quadtree algorithm of BH-SNE as a data-driven quadtree (D-Quadtree).

One-time tree construction (instead of every iteration). Unlike BH-SNE, which builds a quadtree from scratch per iteration, the above-mentioned properties of z_i allow PixelSNE to build P-Quadtree just one time before the main iterations of gradient-descent update and to recycle it during the iterations. That is, PixelSNE pre-computes the full information about (1) the boundary (Eq. (6)) of each cell and (2) its center of mass (Eq. (8)) as follows.

For the boundary information, we utilize the fact that since $\min_i z_{i,d}^{(t)} = 0$ and $\max_i z_{i,d}^{(t)} = r_d$ for every iteration, Eqs. (9) and (10) boil down to

$$\begin{aligned} b_{min,d}^{(c_{root})} &= 0 \text{ and} \\ b_{max,d}^{(c_{root})} &= r_d + \epsilon, \forall d \in \{1, 2\}, \end{aligned}$$

which is no longer dependent on iteration t . This constant boundary of the root node makes those of all the child cells in P-Quadtree constant as well. This results a fixed depth of P-Quadtree as long as the minimum size of the cell is determined, which will be discussed later part of this sub-section in detail. Based on this idea, PixelSNE pre-computes the boundaries of all the cells in P-Quadtree.

Next, since the boundary of each cell is already determined, we simply approximate the center of mass y_c as the center location of the cell corresponding region, e.g.,

$$y_{c,d} = \frac{b_{min,d}^{(c)} + b_{max,d}^{(c)}}{2}, \forall d \in \{1, 2\},$$

which is also not dependent on iteration t .

Once the pre-computation of the above information (Fig. 1(c-1)) finishes, the iterative gradient optimization in PixelSNE simply assigns $z_i^{(t)}$'s to these pre-computed cells in P-Quadtree and updates \mathcal{Y}_c and N_c (Fig. 1(c-2)). Note that in contrast, BH-SNE iteratively computes all these steps every iteration (Figs. 1(b-1) and (b-2)), which acts as the critical inefficiency compared to PixelSNE.

Bounded tree depth based on screen resolution. Considering a typical screen resolution, BH-SNE performs an excessively precise computation. That is, when mapping D-Quadtree to pixel grids of our screen, one can view that BH-SNE subdivides the pixels, the minimum unit of the screen, into much smaller cells until each left cell contains at most one data point (Fig. 1(T-1)).

On the contrary, the minimum size of the cell in P-Quadtree is bounded to the pixel size to avoid an excessive precision in computation (Fig. 1(T-2)). In detail, P-Quadtree keeps splitting the cell c while satisfying the condition,

$$b_{max,d}^{(c)} - b_{min,d}^{(c)} > 1, \exists d \in \{1, 2\},$$

which indicates that the cell length is larger than the unit pixel size 1 for at least one of the two axes. As a result, the depth of P-Quadtree is bounded by

$$\max_{d \in \{1, 2\}} \lceil \log_2 r_d \rceil.$$

Such a bounded depth of P-Quadtree causes a leaf node to possibly contain multiple data points, and in the gradient-descent update step, we may not find the cell satisfying Eq. (11) even after reaching a leaf node in the depth-first search traversal. In this case, we just stop the traversal and use the center of mass of the corresponding leaf node to approximately compute F_{rep} (Eq. (5)) of those points contained in the node.

Finally, let us clarify that we maintain z_i 's as double-precision numbers just as BH-SNE, but our idea of a limited precision is realized mainly by the two above-described novel techniques.

Computational complexity. The depth of the Barnes-Hut tree acts as a critical factor in algorithm efficiency since both the assignment of data point to cells and the approximation of F_{rep} (Eq. (5)) are performed based depth-first search traversal, the computational complexity of which is linear to the tree depth. In the worst case where a majority of data points are located in a relatively small region in a 2D space and a few outliers are located far from them, D-Quadtree can grow as deeply as the depth of N , which is much larger than that of P-Quadtree, $\max_{d \in \{1, 2\}} \lceil \log_2 r_d \rceil$, when $r_d \ll N$, $\forall d \in \{1, 2\}$. Owing to this characteristics, the overall computational complexity of PixelSNE is obtained as $O(N \times \max_{d \in \{1, 2\}} \lceil \log_2 r_d \rceil)$, which reduces to the linear computational complexity in terms of the number of data items, given the fixed screen resolution r_d 's.

Intuitively, BH-SNE traverses much finer-grained nodes to obtain the excessively precise differentiation among data points. On the other hand, PixelSNE assumes that as long as multiple data points are captured within a single pixel, they are close enough to be represented as the center of mass for their visualization in a screen. This guarantees the depth of P-Quadtree to be limited by the screen resolution, instead of being influenced by the undesirable non-uniformity of the 2D embedding results during algorithm iterations.

4.2 Screen-Driven Scaling

In order for the outputs z_i 's at every iteration to satisfy Eq. (2) after their gradient-descent update, we scale them as follows. Let us denote $z_i^{(t-1)}$ as the 2D coordinates computed at iteration $t-1$ and $\hat{z}_i^{(t)}$ as its updated coordinates at the next iteration t via a gradient-descent method. Note that $z_i^{(t-1)}$ satisfies Eq. (2) while $\hat{z}_i^{(t)}$ does

not. Hence, we normalize each of the 2D coordinates of $\hat{z}_i^{(t)}$ and obtain $z_i^{(t)} = \begin{bmatrix} z_{i,1} \\ z_{i,2} \end{bmatrix}$ as

$$z_{i,d}^{(t)} = \frac{r_d \left(\hat{z}_{i,d}^{(t)} - \min_i \hat{z}_{i,d}^{(t)} \right)}{Y_d^{(t)}}, \forall d \in \{1, 2\},$$

where $Y_d^{(t)} = \max_i \hat{z}_{i,d}^{(t)} - \min_i \hat{z}_{i,d}^{(t)} + \epsilon$ and ϵ is a small constant, e.g., 10^{-6} . The reason for introducing ϵ is to have the integer-valued 2D pixel coordinates $\lfloor z_i \rfloor$ in Eq. (1) lie exactly between 0 and $(r_d - 1)$ for $d = 1, 2$. For example, for a 1024×768 resolution, we impose the pixel coordinates at each iteration to exactly have the range from 0 to 1023 and that from 0 to 767 for x - and y -coordinates, respectively.

This scaling step, however, affects the computation of the low-dimensional pairwise probability matrix Q since it scales each pairwise Euclidean distance, $\|y_i - y_j\|$, in Eq. (3), resulting in a different probability distribution from the case with no scaling. To compensate this scaling effect in computing Q , we re-define Q with respect to the scaled z_i 's as

$$q_{ij}^{(t)} = \left(\left(1 + \sum_{d=1}^2 \beta_d^{(t)} \left(z_{i,d}^{(t-1)} - z_{j,d}^{(t-1)} \right)^2 \right) Z^{(t)} \right)^{-1} \quad (12)$$

where $Z^{(t)} = \sum_{k \neq l} \left(1 + \sum_{d=1}^2 \beta_d^{(t)} \left(z_{i,d}^{(t-1)} - z_{j,d}^{(t-1)} \right)^2 \right)^{-1}$ and β_d is defined as

$$\beta_d^{(t)} = \prod_{s=1}^{t-1} \left(\frac{Y_d^{(s)}}{r_d} \right)^2, \forall d \in \{1, 2\}. \quad (13)$$

where $Y_d^{(1)} = \epsilon$, since $\hat{z}_i^{(1)}$ is randomly initialized from $\mathcal{N}(0, 1)$. By introducing $\beta_d^{(t)}$ defined in this manner, PixelSNE uses Eq. (12), which is still equivalent to Eq. (3).

4.3 Accelerating Construction of P

To accelerate the process of constructing the matrix P , we adopt a recently proposed, highly efficient algorithm of constructing the approximate k -nearest neighbor graph (K-NNG) [19]. This algorithm builds on top of the classical state-of-the-art algorithm based on random-projection trees but significantly improves its efficiency. It first starts with a few random projection trees to construct an approximate K-NNG. Afterwards, based on the intuition that ‘‘the neighbors of my neighbors are also likely to be my neighbors,’’ the algorithm iteratively improves the accuracy of K-NNG by exploring the neighbors of neighbors defined according to the current K-NNG. In our experiments, we show that this algorithm is indeed able to significantly accelerate the process of constructing P .

4.4 Implementation Improvements

The implementation of PixelSNE is built upon that of BH-SNE publicly available at <https://github.com/lvdmaaten/bhtsne>. Other than the above algorithmic improvements, we made implementation improvements as follows.

First, the Barnes-Hut tree involves many computations of division by two (or powers of two). We replaced such computations by more efficient, bitwise left-shift operations. Similarly, we replaced

modulo-two operations, which is used in data point assignment to cells, with bitwise masking with 0×0001 . Finally, we replaced the ‘pow’ function from ‘math’ library in C/C++, which is used for squared-distance computation with a single multiplication, e.g., $x \times x$ instead of ‘pow($x, 2$)’. Although not significant, these implementation modifications rendered consistently faster computing times than the case without them.

5 EXPERIMENTS

In this section, we present the quantitative analyses as well as qualitative visualization examples of PixelSNE in comparison with original t-SNE and BH-SNE. All the experiments were conducted on a single desktop computer with Intel Core i7-6700K processors, 32GB RAM, and Ubuntu 16.04.1 LTS installed.

5.1 Experimental Setup

This section describes our experimental setup including datasets and compared methods.

5.1.1 Datasets. Our experiments used four real-world datasets as follows: (1) **MNIST** digit images, (2) Facial expression images (**FaceExp**), (3) 20 Newsgroups documents (**20News**), (4) News aggregator dataset (**NewsAgg**) and (5) **Yelp** reviews.

MNIST² dataset contains a set of 70,000 gray-scale handwritten digit images with $28 \times 28 = 784$ pixels, resulting in an input matrix $\mathcal{X} \in \mathbb{R}^{784 \times 70,000}$. Each image has its digit label among ten different digits.

FaceExp³ dataset contains a set of 28,709 gray-scale facial image data with 48×48 pixels, with the label information out of seven different facial expression categories. For this dataset, we extracted the features from each image using a convolutional neural network. This network starts with four convolutional layers with the 32, 64, 96, and 128 filters, respectively, with the size of each filter being 3×3 . Each convolutional layer is followed by the batch normalization layer, rectified linear unit (ReLU), and the max-pooling layer over 2×2 patches. After then, two fully connected layers follow: the first one with 256 output nodes followed by ReLU and the second with 256 output nodes followed by a softmax classifier for seven facial expression categories. After training this model, we used the last hidden layer output of 256 dimensions as the feature vector of each image, resulting in an input matrix $\mathcal{X} \in \mathbb{R}^{256 \times 28,709}$.

20News⁴ dataset is a collection of 18,846 newsgroup posts on 20 different newsgroup categories. We used the label of each document as one of seven higher-level newsgroup categories. From each document, we extracted the embedding vectors of those words in it using a pre-trained word2vec embedding vector⁵ and then averaged them to represent a single document, resulting in an input matrix $\mathcal{X} \in \mathbb{R}^{300 \times 18,846}$.

NewsAgg⁶ dataset contains a collection of 421,161 news headlines on four different categories. We represent the each headline with the averaged words vector pre-processed as explained above. This results in an input matrix $\mathcal{X} \in \mathbb{R}^{300 \times 421,161}$.

²<http://cs.nyu.edu/~roweis/data.html>

³<https://goo.gl/W3Z8qZ>

⁴<http://qwone.com/~jason/20Newsgroups/>

⁵<https://github.com/mmihaltz/word2vec-GoogleNews-vectors>

⁶<https://www.kaggle.com/uciml/news-aggregator-dataset>

Table 1: Comparison of computing times among 2D embedding algorithms. The t-SNE results are excluded for large datasets due to its long computing time. The total computing times are shown in boldface, and the numbers in parentheses represent the standard deviation from three repetitions.

	20News			FacExp			MNIST			NewsAgg			Yelp		
	<i>P</i>	Coord	Total	<i>P</i>	Coord	Total	<i>P</i>	Coord	Total	<i>P</i>	Coord	Total	<i>P</i>	Coord	Total
t-SNE	2.43m (0.98s)	36.87m (55.08s)	39.31m (56.06s)	6.48m (0.23s)	84.94m (10.12s)	91.41m (10.13s)	(-)	(-)	(-)	(-)	(-)	(-)	(-)	(-)	(-)
BH-SNE	22.25s (1.55s)	156.70s (6.62s)	178.95s (8.16s)	0.19m (0.84s)	5.48m (40.73s)	5.56m (39.89s)	5.10m (10.84s)	13.93m (2.27m)	19.03m (2.45m)	3.96h (7.05m)	1.81h (4.04m)	5.77h (11.45m)	12.44h (19.29m)	5.83h (17.93m)	18.27h (37.22m)
PixelSNE-VP	14.68s (1.46s)	70.71s (1.58s)	85.39s (3.03s)	0.14m (0.66s)	2.04m (3.52s)	2.19m (4.16s)	3.76m (16.48s)	6.17m (11.92s)	9.92m (28.37s)	2.84h (5.49m)	0.63h (1.04m)	3.46h (6.52m)	8.89h (14.26m)	3.11h (7.47m)	12.00h (21.71m)
PixelSNE-RP	15.53s (0.49s)	72.17s (1.44s)	87.70s (1.93s)	0.32m (1.44s)	2.04m (3.57s)	2.36m (4.99s)	1.40m (2.22s)	6.05m (7.81s)	7.45m (9.86s)	0.30h (0.43m)	0.63h (2.08m)	0.94h (2.50m)	0.76h (0.97m)	3.14h (10.23m)	3.90h (11.20m)

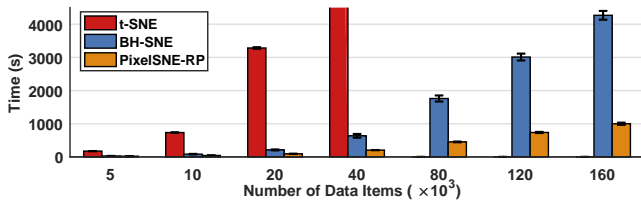


Figure 2: Computing times vs. the number of data items on NewsAgg dataset. The error bar represents the standard deviation from five repetitions. The t-SNE results are excluded for large datasets due to its long computing time.

Yelp⁷ review dataset contains around 2.7 million reviews written by around 687,000 users. We pre-processed this dataset by removing those rare keywords appearing in less than 20 documents and other general keywords such as food, restaurant, etc. After forming a term-document matrix, we randomly selected one million reviews from it, resulting in an input matrix $X \in \mathbb{R}^{33,706 \times 1,000,000}$. Afterwards, we extracted topic labels out of ten topics computed by nonnegative matrix factorization [13] as a topic modeling method.

For all datasets, we reduced the dimensionality, i.e.g, the number of rows of each input matrix to 50 by applying PCA, which is a standard pre-processing step of t-SNE and BH-SNE.

5.1.2 Compared Methods. We compared our methods against the original t-SNE and BH-SNE. For both methods, we used the publicly available code written by the original author.⁸ We used the default parameter values for both methods, e.g., the perplexity value as 50, the number of iterations as 1,000, and the threshold θ in Eq. (11) as 0.5.

For our PixelSNE, we used its two different versions depending on the algorithm for constructing P : (1) the vantage-point tree (PixelSNE-VP) used originally in BH-SNE and (2) the random projection tree-based approach (PixelSNE-RP) used in LargeVis [19] (Section 4.3). For the latter, we extracted the corresponding part called k -nearest neighbor construction from the publicly available code⁹ and integrated it with our implementation of PixelSNE with

⁷https://www.yelp.com/dataset_challenge

⁸<https://lvdmaaten.github.io/tsne/>

⁹<https://github.com/lferry007/LargeVis>

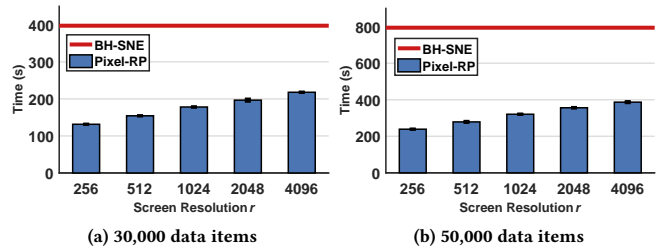


Figure 3: Computing times of BH-SNE and PixelSNE-RP with the different screen resolutions on MNIST dataset. The error bar represents the standard deviation from five repetitions.

its default parameter settings except for setting the number of threads as 1 to exclude the effect of parallelism. We set the number of iterations and the threshold θ in Eq. (11) as the same as BH-SNE, e.g., 1,000 and 0.5, respectively. We set both of the screen resolution parameters r_1 and r_2 as 512 for 20News and FacExp datasets. For MNIST, NewsAgg and Yelp datasets, both are set as 1024, 2048 and 8192, respectively.

5.2 Computing Time Analysis

Table 1 shows the comparison of computing times of various algorithms for different datasets. We report the computing time of two sub-routines as well as their total times: (1) constructing the original pairwise probability matrix P (**P**), (2) optimizing low-dimensional coordinates (**Coord**), and (3) the total computing time (**Total**). For fair comparisons, the minor improvements presented in Section 4.4 are not applied to PixelSNE-VP nor to PixelSNE-RP. In addition, due to its significant computing time, the computation time results of t-SNE is excluded for large datasets such as Yelp or NewsAgg datasets.

Comparison results. In all cases, PixelSNE-VP and PixelSNE-RP consistently outperform t-SNE and BH-SNE by a large margin. For example, for Yelp dataset, BH-SNE took more than 18 hours while PixelSNE-VP and PixelSNE-RP took 12 hours and less

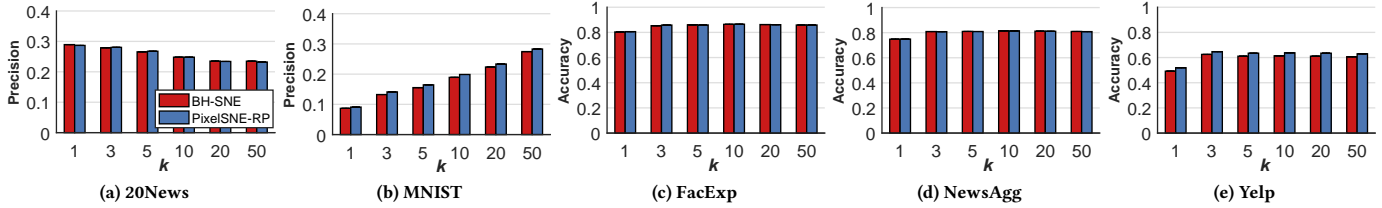


Figure 4: Embedding quality comparisons between BH-SNE and PixelSNE-RP. We report the neighborhood precision (Eq. (14)) for (a) and (b) and the k -NN classification accuracy for (c), (d), and (e).

than 4 hours, respectively. For the part of optimizing the low-dimensional coordinates (**Coord**), where we mainly applied our screen resolution-driven precision, PixelSNE-RP and PixelSNE-VP both show the significant performance boost against BH-SNE. For instance, PixelSNE-VP and PixelSNE-RP compute this part more than three times faster than BH-SNE for NewsAgg dataset. When it comes to the part of constructing $P(P)$, as the size of the data gets larger, e.g., NewsAgg and Yelp datasets, PixelSNE-RP runs significantly faster than PixelSNE-VP due to the advantage of random projection tree adopted in PixelSNE (Section. 4.3).

Scalability due to the data size. Next, Fig. 2 shows the computing times depending on the total number of data items, sampled from NewsAgg dataset. As the data size gets larger, our PixelSNE-RP runs increasingly faster than BH-SNE as well as t-SNE, which shows the promising scalability of PixelSNE.

Effects of the precision parameter. Fig. 3 shows the computing time depending on the screen resolution parameter r for 30,000 and 50,000 random samples from MNIST dataset. Although PixelSNE-RP is consistently faster than BH-SNE, it tends to run slowly as r increases. Nonetheless, our method still runs much faster, e.g., around two-fold speedup compared to BH-SNE, even with a fairly large values of r , i.e. 4,096, which can contain more than 16 million pixels.

Effects of implementation improvements. We compared the computing time between PixelSNE-RP and improved PixelSNE-RP, which adopts the efficient operation proposed in Section 4.4. Table. 2 presents that the improved version consistently brings around 4% speed improvement compared to the original PixelSNE-RP for all the datasets. Interestingly, our improvement also reduces the variance of computing times.

Table 2: Computing times of PixelSNE-RP with and without the improvements shown in Section 4.4). The numbers in the parentheses represent the standard deviation from three repetitions.

	20News	FecExp	MNIST	NewsAgg	Yelp
Improved PixelSNE-RP (Sec. 4.4)	83.26s (0.19s)	134.43s (0.21s)	429.08s (9.05s)	3194.86s (38.99s)	13485.27s (51.1s)
PixelSNE-RP	87.7s (1.93s)	141.54s (4.99s)	446.88s (9.86s)	3370.36s (150.04s)	14025.12s (671.84s)

Table 3: Neighborhood precision (Eq. (14)) of PixelSNE-RP on the 10,000 samples of MNIST dataset. The numbers in the parentheses represent the standard deviation from ten repetitions.

r	k in k nearest neighbors					
	1	3	5	10	20	30
512	.2401 (.0125)	.3207 (.0117)	.3475 (.0098)	.3719 (.0064)	.3916 (.0033)	.4237 (.0023)
1024	.2405 (.0084)	.3165 (.0077)	.3434 (.0061)	.3702 (.0037)	.3932 (.0023)	.4290 (.0011)
2048	.2463 (.0056)	.3216 (.0045)	.3481 (.0046)	.3750 (.0030)	.3977 (.0022)	.4328 (.0008)
4096	.2517 (.0054)	.3272 (.0052)	.3532 (.0046)	.3782 (.0027)	.4006 (.0018)	.4344 (.0009)

5.3 Embedding Quality Analysis

Evaluation measures. To analyze the embedding quality we adopted the two following measures:

Neighborhood precision measures how much the k original nearest neighbors in a high-dimensional space are captured in the k nearest neighbors in the 2D embedding results. In detail, let us denote the k nearest neighbors of data i in the high-dimensional space and those in the low-dimensional (2D) space as $\mathcal{N}_D^{(k)}(i)$ and $\mathcal{N}_d^{(k)}(i)$, respectively. The neighborhood precision is computed as

$$\frac{1}{kN} \sum_{i=1}^N \left| \mathcal{N}_D^{(k)}(i) \cap \mathcal{N}_d^{(k)}(i) \right| \quad (14)$$

k -NN classification accuracy measures the k -nearest neighbor classification accuracy based on the 2D embedding results along with their labels.

Method comparisons. Fig. 4 shows the comparison results between PixelSNE-RP and BH-SNE depending on different k values. For the neighborhood precision measure, PixelSNE-RP achieves the similar or even better performance compared to the BH-SNE (Figs. 4(a) and (b)). We conjecture the reason is because the random projection tree used in PixelSNE-RP (Section 4.3) finds more accurate nearest neighbors than the vantage-point tree used in BH-SNE [19]. For k -NN classification accuracy results shown in Figs. 4(c)-(e), the performance gap between the two are small, indicating that our method has a comparable quality of outputs to BH-SNE.

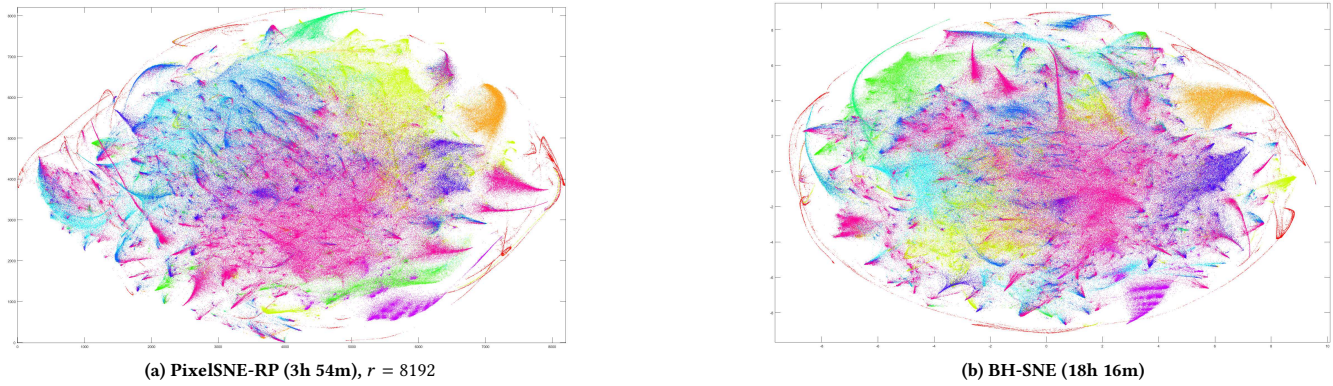


Figure 5: 2D embedding of Yelp dataset. The numbers in parentheses indicate the computing time.

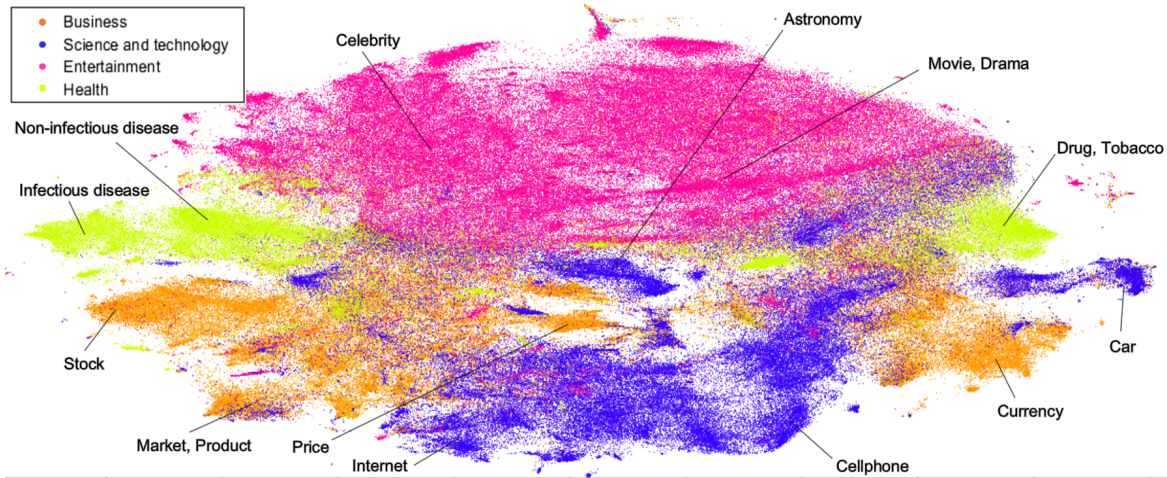


Figure 6: 2D embedding of NewsAgg dataset generated by PixelSNE-RP.

Table 4: k -NN classification accuracy of PixelSNE-RP on the 10,000 samples of MNIST dataset. The numbers in parentheses represent the standard deviation from ten repetitions.

r	k in k nearest neighbors					
	1	3	5	10	20	30
512	.9390 (.0012)	.9482 (.0023)	.9463 (.0023)	.9428 (.0023)	.9367 (.0033)	.9297 (.0045)
1024	.9387 (.0017)	.9489 (.0023)	.9475 (.0014)	.9450 (.0014)	.9400 (.0011)	.9335 (.0017)
2048	.9386 (.0020)	.9489 (.0018)	.9472 (.0011)	.9395 (.0020)	.9450 (.0014)	.9323 (.0015)
4096	.9380 (.0018)	.9484 (.0007)	.9471 (.0013)	.9437 (.0013)	.9382 (.0014)	.9324 (.0019)

Effects of the precision parameter. Tables 3 and 4 show the above two measures for PixelSNE-RP with respect to different values of a screen resolution r . Unlike the k -NN classification accuracy, which stays roughly the same regardless of different values of r ,

the neighborhood precision consistently increases as r gets large. However, the gap is not that significant.

Cost value analysis. Finally, Table 5 compares the cost function value (Eq. (4)) after convergence. Considering the baseline cost value of the random initialization, both BH-SNE and PixelSNE-RP achieved a similar level of the algorithm objective. Also, throughout all the values of r tested, this value remains almost the same between BH-SNE and PixelSNE-RP, which indicates that the screen resolution-based precision of PixelSNE has minimal to no impact in achieving the optimal cost value, which is consistent with the results found in Tables 3 and 4.

Table 5: Comparison of cost function values between BH-SNE and PixelSNE-RP. The numbers in parentheses represent the standard deviation from ten repetitions.

	Random Coordinates	BH-SNE	PixelSNE-RP (with r)			
			512	1024	2048	4096
Cost value (Eq. 4)	91.580 (.000)	1.815 (.0071)	1.820 (.0303)	1.865 (.0167)	1.871 (.0113)	1.868 (.0167)

5.4 Exploratory Analysis

Finally, we present visualization examples for Yelp and NewsAgg datasets.¹⁰ Fig. 5 presents the visualization generated from PixelSNE-RP and BH-SNE on Yelp dataset. Different colors represent ten different labels generated from topic modeling. Even though PixelSNE-RP ran 4.7 times faster than BH-SNE, the visualization results are comparable to each other.

Fig. 6 shows the visualization result on NewsAgg dataset from PixelSNE-RP. A data point, which corresponds to a news headline, is labeled with four different categories: Business, Science and Technology, etc., denoted by different color. Although all the headlines are categorized into only four subjects, Fig. 6 revealed the additional sub-category information by closely embedding news with the similar topics. Each topic is connected with the relevant area as shown in Fig. 6. For example, those news belonging to Health category are roughly divided into three parts, as follow. The topical region “Infectious disease” on the left side consists of the headline with the keywords such as “Ebola”, “West Nile virus” or “Mers” while the region connected with “Non-infectious disease” has headlines with the keywords of “Breast cancer”, “Obesity” or “Alzheimer”. The topical area of “Drug”, “Tobacco” has news about health-related life styles, e.g., “Mid-life Drinking Problem Doubles Later Memory Issues”. Note that the topical regions of “Infectious disease” and “Non-infectious disease” are closely located compared to the other regions.

Another interesting observation is that as long as news headlines even from different categories share similar keywords, they are closely located to each other. For example, the topic cluster of “Market” and “Product”, on the lower-left region contains news from Business and Science and technology. However, it turns out that the news from Science and technology category has the headlines about the stock price of the electronic company or the sales of the electronic products, which is highly related to the headline about the stock market and company performance from Business category.

6 CONCLUSIONS

In this paper, we presented a novel idea of exploiting the screen resolution-driven precision as the fundamental framework for significantly accelerating the 2D embedding algorithms. Applying this idea to a state-of-the-art method called Barnes-Hut SNE, we proposed a novel approach called PixelSNE as a highly efficient alternative.

In the future, we plan to apply our framework to other advanced algorithms such as LargeVis [19]. We also plan to develop a parallel distributed version of PixelSNE to further improve the computational efficiency.

REFERENCES

- [1] Josh Barnes and Piet Hut. 1986. A hierarchical $O(N \log N)$ force-calculation algorithm. *nature* 324, 6096 (1986), 446–449.
- [2] Mikhail Belkin and Partha Niyogi. 2003. Laplacian Eigenmaps for Dimensionality Reduction and Data Representation. *Neural Computation* 15, 6 (2003), 1373–1396.
- [3] Christopher M Bishop, Markus Svensén, and Christopher KI Williams. 1998. GTM: The generative topographic mapping. *Neural computation* 10, 1 (1998), 215–234.

- [4] Miguel A Carreira-Perpinán. 2010. The Elastic Embedding Algorithm for Dimensionality Reduction. In *Proc. the International Conference on Machine Learning (ICML)*, 167–174.
- [5] Jaegul Choo and Haesun Park. 2013. Customizing Computational Methods for Visual Analytics with Big Data. *IEEE Computer Graphics and Applications (CG&A)* 33, 4 (2013), 22–28.
- [6] A. Gisbrecht, B. Mokbel, and B. Hammer. 2012. Linear basis-function t-SNE for fast nonlinear dimensionality reduction. In *Proc. the International Joint Conference on Neural Networks (IJCNN)*, 1–8.
- [7] Geoffrey E Hinton and Sam T Roweis. 2002. Stochastic neighbor embedding. In *Advances in neural information processing systems*, 833–840.
- [8] G. E. Hinton and R. R. Salakhutdinov. 2006. Reducing the Dimensionality of Data with Neural Networks. *Science* 313, 5786 (2006), 504–507.
- [9] Ian T. Jolliffe. 2002. *Principal component analysis*. Springer.
- [10] T. Kohonen. 2001. *Self-organizing maps*. Springer.
- [11] J. Kruskal. 1964. Multidimensional scaling by optimizing goodness of fit to a nonmetric hypothesis. *Psychometrika* 29 (1964), 1–27. Issue 1.
- [12] J. Kruskal. 1964. Nonmetric multidimensional scaling: A numerical method. *Psychometrika* 29 (1964), 115–129. Issue 2.
- [13] D. D. Lee and H. S. Seung. 1999. Learning the parts of objects by non-negative matrix factorization. *Nature* 401 (1999), 788–791.
- [14] John A Lee and Michel Verleysen. 2007. *Nonlinear dimensionality reduction*. Springer Science & Business Media.
- [15] Laurens Maaten. 2009. Learning a Parametric Embedding by Preserving Local Structure. In *Proc. the International Conference on Artificial Intelligence and Statistics (AISTATS)*, Vol. 5. 384–391.
- [16] N. Pezzotti, B. Lelieveldt, L. van der Maaten, T. Hollt, E. Eisemann, and A. V. Ivanova. 2016. Approximated and User Steerable tSNE for Progressive Visual Analytics. *IEEE Transactions on Visualization and Computer Graphics (TVCG)* PP, 99 (2016), 1–1.
- [17] Jr. Sammon, John W. 1969. A Nonlinear Mapping for Data Structure Analysis. *Computers, IEEE Transactions on C-18*, 5 (may. 1969), 401 – 409.
- [18] L. K. Saul and S. T. Roweis. 2003. Think Globally, Fit Locally: Unsupervised Learning of Low Dimensional Manifolds. *Journal of Machine Learning Research (JMLR)* 4 (2003), 119–155.
- [19] Jian Tang, Jingzhou Liu, Ming Zhang, and Qiaozhu Mei. 2016. Visualizing Large-scale and High-dimensional Data. In *Proc. the International Conference on World Wide Web (WWW)*, 287–297.
- [20] Joshua B. Tenenbaum, Vin de Silva, and John C. Langford. 2000. A Global Geometric Framework for Nonlinear Dimensionality Reduction. *Science* 290, 5500 (2000), 2319–2323. DOI: <http://dx.doi.org/10.1126/science.290.5500.2319> arXiv:<http://www.sciencemag.org/cgi/reprint/290/5500/2319.pdf>
- [21] Laurens Van Der Maaten. 2014. Accelerating t-SNE using tree-based algorithms. *Journal of machine learning research (JMLR)* 15, 1 (2014), 3221–3245.
- [22] L. van der Maaten and G. Hinton. 2008. Visualizing data using t-SNE. *Journal of Machine Learning Research (JMLR)* 9 (2008), 2579–2605.
- [23] Laurens van der Maaten and Geoffrey Hinton. 2012. Visualizing non-metric similarities in multiple maps. *Machine Learning* 87, 1 (2012), 33–55.
- [24] LJP Van der Maaten, EO Postma, and HJ Van den Herik. 2009. Dimensionality reduction: A comparative review. *Technical Report TiCC TR 2009-005* (2009).
- [25] L. van der Maaten and K. Weinberger. 2012. Stochastic triplet embedding. In *IEEE International Workshop on Machine Learning for Signal Processing*, 1–6.
- [26] Jarkko Venna, Jaakko Peltonen, Kristian Nybo, Helena Aidos, and Samuel Kaski. 2010. Information retrieval perspective to nonlinear dimensionality reduction for data visualization. *Journal of Machine Learning Research (JMLR)* 11, Feb (2010), 451–490.
- [27] Kilian Weinberger and Lawrence Saul. 2006. Unsupervised Learning of Image Manifolds by Semidefinite Programming. *International Journal of Computer Vision* 70 (2006), 77–90. Issue 1.
- [28] Peter N Yianilos. 1993. Data structures and algorithms for nearest neighbor search in general metric spaces. In *Proc. the ACM-SIAM Symposium on Discrete Algorithms (SODA)*, 311–21.

¹⁰High-resolution images and other comparison results are available at http://davian.korea.ac.kr/myfiles/jchoo/resource/kdd17pixelsne_appendix.pdf.